

Precrystallization of fluids induced by patterned substrates

Martin Heni and Hartmut Löwen

Institut für Theoretische Physik II, Heinrich-Heine-Universität Düsseldorf, Universitätsstrasse 1, 40225 Düsseldorf, Germany

Received 8 December 2000, in final form 7 February 2001

Abstract

It is shown that a fluid near a topographically patterned wall exhibits crystallization below the bulk freezing point (so-called precrystallization). In detail, a periodic array of fixed hard spheres is considered as a wall pattern. The actual type of the pattern corresponds to a face-centred-cubic (fcc) lattice cut along the (111), (100) or (110) orientation, a hexagonal-close-packed (hcp) solid with (110) orientation as well as a rhombic lattice distorted with respect to the triangular one. The fluid is represented by mobile hard spheres of the same diameter as the fixed wall spheres. By computer simulation we find complete wetting by a crystalline sheet proceeding via a cascade of layering transitions as the bulk freezing point is approached for the fcc (111) and hcp (110) cases, provided that the wall crystal lattice exactly matches that of the coexisting bulk crystal. On the other hand, there is incomplete wetting for the fcc (100) and (110) cases. The freezing of the first layer starts at *lower* bulk pressures for a lattice with a larger lattice constant as compared to that of the coexisting bulk crystal. A rhombic pattern either results in incomplete wetting by a solid sheet, which is unstable as a bulk phase, or prevents wetting completely. Using a phenomenological theory we derive scaling relations for the thickness of the crystalline layer which are confirmed by the simulation data. We furthermore show that the Lindemann rule of bulk freezing can be applied also for interfacial freezing transitions.

1. Introduction

Liquids at interfaces can exhibit structural changes and thermodynamic interfacial phase transitions which are much more subtle than their bulk behaviour. One important phenomenon is wetting [1, 2] which is interesting from a fundamental point of view but also has many important applications. A special type of wetting transition is present if the wetting phase is crystalline. Examples include precrystallization for hard-sphere fluids near smooth walls [3, 4], surface freezing [5–9] as found for alkanes [10–16] and alcohols [17, 18] and triple-point wetting of rare gases on metallic substrates [19].

In this paper we focus on the wall-induced precrystallization of hard-sphere fluids which was found to occur very close to coexistence for a *smooth* wall [3,4]. We show that the surface pattern plays a decisive role in determining the details of the wetting scenario. Depending on the pattern there can be either complete wetting, incomplete wetting or no precrystallization at all. Our work is motivated by the recent development of lithographic techniques by means of which chemical and topological wall patterns can be imprinted onto a substrate. A profound influence on the wetting behaviour of fluids on patterned substrates was found as in other recent studies [20–23].

In our model we focus on a fluid of spherical particles modelled as hard spheres in the neighbourhood of a substrate composed of fixed hard spheres forming a periodic two-dimensional array. There are two main reasons for our approach. First, the model is kept simple since the thermodynamics and phase diagram of the bulk hard-sphere system depend only on the bulk volume fraction η . Understanding the molecular principles of precrystallization is thus possible within this ‘minimal’ framework. Second, our model is actually applicable for index-matched sterically stabilized colloidal suspensions on periodic patterned substrates which can be prepared by ‘gluing’ colloidal spheres onto a periodic pattern [24–26]. Such colloidal model systems bear the further advantage that real-space experiments can be performed as the relevant length scale is shifted from the microscopic to the mesoscopic regime [27]. Nevertheless our model may also serve as a simple microscopic description of molecular systems such as liquid metals on crystalline surfaces. Consequently, all of our predictions can in principle be verified in real-space experiments on colloidal suspensions [28–31] or by scattering techniques probing the inhomogeneous microscopic structure of liquid metals near crystalline substrates [32].

By computer simulation we show that a pattern which is commensurate with the bulk crystal can ignite complete precrystallization with an onset far away from bulk coexistence. This proceeds via a cascade of subsequent layering transitions as the bulk freezing transition is approached. However, whether there is complete or incomplete precrystallization depends on the type of the surface pattern. A triangular lattice produces complete wetting while a square lattice gives only incomplete wetting. On the other hand, a surface pattern which is distorted from the compatible one leads either to incomplete wetting or prevents wetting completely. For small distortions there is incomplete wetting by crystalline layers which are unstable as a bulk phase. These layers directly inherit their structure from the underlying pattern. However, above a critical distortion, precrystallization does not occur any longer. Furthermore, we show that precrystallization can be tuned by a mismatch of the substrate pattern with respect to the coexisting bulk crystal. For larger substrate lattice spacing, the first layer crystallizes at lower bulk pressures.

Our simulation results are in quantitative agreement with scaling relations derived from a simple phenomenological theory. Parts of this work we have already published elsewhere [33].

The paper is organized as follows. In section 2 we describe our model. A simple phenomenological approach is presented in section 3. Then we describe the simulation procedure in sections 4 to 6. In particular, we identify a suitable order parameter for detecting layer-resolved precrystallization in section 5. Results are presented and discussed in section 7 while section 8 is devoted to conclusions.

2. The model

We consider N hard spheres with diameter σ in a large volume V at a fixed temperature T . The number density of the spheres is $\rho = N/V$ which can be conveniently expressed in terms of the dimensionless packing fraction $\eta = \pi\rho\sigma^3/6$. For excluded-volume interactions, the temperature only sets the energy scale $k_B T$ (k_B denoting Boltzmann’s constant) and does not

affect the phase transitions or structural correlations. Hence the bulk system is completely specified by the bulk packing fraction η . It is well established [34] that the bulk hard-sphere system exhibits a first-order freezing transition from a fluid phase to a face-centred-cubic (fcc) crystal [35]. The coexisting densities are $\rho \equiv \rho_f = 0.943/\sigma^3$ for the fluid and $\rho \equiv \rho_s = 1.041/\sigma^3$ for the solid; the packing fractions are $\eta \equiv \eta_f = 0.494$ for the fluid and $\eta \equiv \eta_s = 0.545$ for the solid. The scaled pressure $P^* = P\sigma^3/k_B T$ at coexistence is $P_c^* = 11.64$.

In detail, the centre-of-mass positions of the spheres are denoted by $\vec{r}_i = (x_i, y_i, z_i)$ ($i = 1, \dots, N$). Two hard spheres i and j interact via the pair potential

$$U(\vec{r}_i, \vec{r}_j) = \begin{cases} \infty & \text{if } |\vec{r}_i - \vec{r}_j| < \sigma \\ 0 & \text{otherwise.} \end{cases} \quad (1)$$

In the following we include a surface in the hard-sphere system. The presence of such a surface is described by an additional external potential which in general can model any wall pattern. Yet to simplify the model this interaction is modelled as N_w fixed hard spheres interacting with the mobile ones with the potential from equation (1) which acts on the centres of the i th hard sphere ($i = 1, \dots, N$) and the j th wall particle $j = 1, \dots, N_w$. The actual wall area is A and the positions of the fixed spheres on the given lattice are denoted by $\{\vec{r}_j^w\}$.

In the following we will concentrate on a few selected wall structures which are either interesting for experiments or which show a generic behaviour. We choose the triangular wall pattern, resulting from a cut along the (111) plane of a fcc crystal, as it is intuitively the most favourable surface that we can offer for a solid. This substrate pattern is shown in figure 2(a)—see below. It corresponds to a triangular crystal whose lattice constant $a_\Delta = 1.1075\sigma$ matches the coexisting bulk crystal. With this example we investigate in detail the effects of a strained crystal by distorting this pattern to form a rhombic crystal. This rhombic pattern can be derived from the ideal triangular one by squeezing the particles in the x -direction and stretching them in the y -direction as depicted in figure 1. a_Δ is the ideal lattice spacing from the triangular pattern, $h_\Delta = \sqrt{3}/2$ and a and h are the lattice spacing of the distorted wall pattern in the x - and y -directions. This leads to strain tensor components $\epsilon_x = (a - a_\Delta)/a_\Delta$ and $\epsilon_y = (h - h_\Delta)/h_\Delta$ with all other components being zero. For our analysis we restrict ourselves to systems where the surface area $A_c = A_\Delta$ of the original and the distorted unit cell at the wall is constant. The advantage of doing so is that this strain leads to a simplified form of the elastic energy as

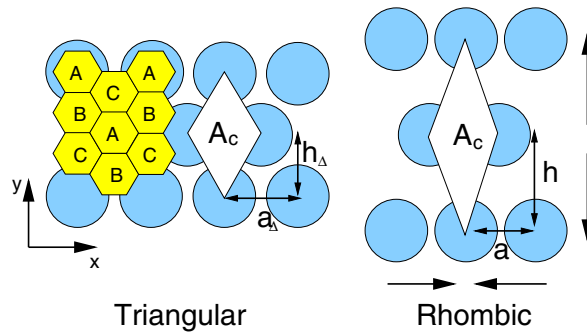


Figure 1. The geometry of the triangular and rhombic substrate patterns. The rhombic pattern results from the triangular one by distorting the lattice as indicated by the arrows such that the area A_c of the unit cell remains constant. For the triangular pattern the three types, A, B and C, of honeycomb cells defining the stacking order parameter are also shown.

we obtain

$$A_{\Delta} \equiv a_{\Delta} h_{\Delta} = a_{\Delta}(1 + \epsilon_x) h_{\Delta}(1 + \epsilon_y) \equiv A_c. \quad (2)$$

Equation (2) gives a relationship between the two strain tensor components ϵ_x and ϵ_y which allows us to define the distortion with only one dimensionless strain parameter:

$$\epsilon = \sqrt{\left(\frac{a - a_{\Delta}}{a_{\Delta}}\right)^2 + \left(\frac{h - h_{\Delta}}{h_{\Delta}}\right)^2}. \quad (3)$$

Furthermore, we study the effects of a lattice constant mismatch within this example. This is done by assuming a unit cell which is shrunk or grown in comparison to the ideal one by a relative distortion which is equal in the x - and y -directions. Although not keeping the surface area constant, we can again define the distortion using one dimensionless strain parameter

$$\epsilon = \sqrt{2} \frac{a - a_{\Delta}}{a_{\Delta}} = \sqrt{2} \frac{h - h_{\Delta}}{h_{\Delta}}. \quad (4)$$

Another type of wall pattern which we investigate is a square wall pattern which is generated by cutting a fcc crystal along the (100) plane as depicted in figure 2(b). This results in a square lattice of fixed spheres. We consider that the lattice constant $a_{\square} = 1.1075\sigma$ exactly matches the coexisting bulk crystal but again include the effects of a slight lattice constant mismatch within this example, as this is of particular experimental interest. In the same way as in equation (4) we define the relative distortion which will be equal in the x - and y -directions as

$$\epsilon = \sqrt{2} \frac{a - a_{\square}}{a_{\square}} = \sqrt{2} \frac{h - h_{\square}}{h_{\square}}. \quad (5)$$

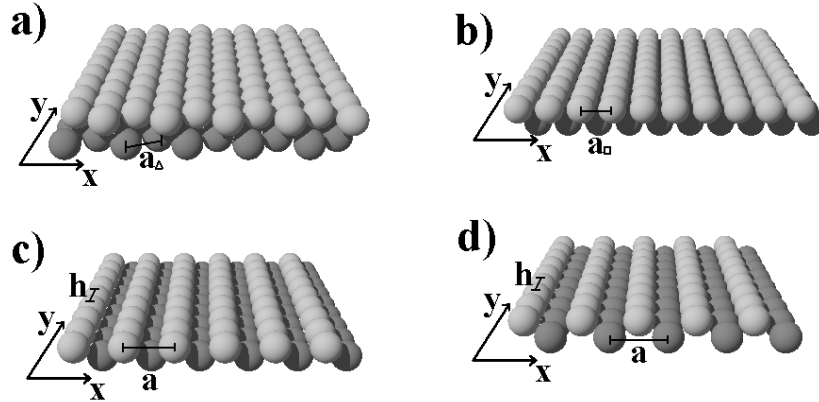


Figure 2. A sketch of different wall patterns: (a) a fcc (111) (triangular) wall pattern with lattice constant $a_{\Delta} = 1.1075\sigma$; (b) a fcc (100) (square) wall pattern with lattice constant $a_{\square} = 1.1075\sigma$; (c) a fcc (110) wall pattern with lattice constants $h = 1.1075\sigma$ and $a = \sqrt{3}h$; (d) a hcp (110) zigzag wall pattern with lattice constants $h = 1.1075\sigma$ and $a = \sqrt{2}h$.

Furthermore, we investigate a pattern made out of linear rows by cutting a hexagonal-close-packed (hcp) as well as a fcc crystal along the (110) plane as shown in figure 2(c) and figure 2(d). We again exactly match the lattice constants to the coexisting bulk crystal. This leads to wall patterns which are quite tightly packed particles in one direction with a separation of $h = 1.1075\sigma$ forming one-dimensional rows. These rows represent a zigzag structure relative to each other; the spacing in the other direction is $a = \sqrt{3}a_{\Delta}$ for the hcp (110) pattern and $a = \sqrt{2}a_{\Delta}$ for the fcc (110) pattern—see figure 2(c) and figure 2(d). These substrate patterns are interesting from an experimental point of view [36].

3. Phenomenological theory

Let us now describe a phenomenological theory for wetting by a crystalline layer. The key quantity of any wetting theory [1] is the difference Σ of the grand canonical free energies per unit area for a wetting and a non-wetting situation. This quantity is discussed as a function of the thermodynamic and system parameters and the width ℓ of the adjacent solid sheet. Minimizing Σ with respect to ℓ yields the equilibrium profile provided that the quantity Σ evaluated at its minimum is negative. There are several contributions to the total free energy Σ resulting from bulk and surface thermodynamics as well as effective interface interactions and free-energy penalties resulting from elastic distortions of the solid. Therefore Σ splits into three terms:

$$\Sigma = \Sigma_1 + \Sigma_2 + \Sigma_3 \quad (6)$$

which we will subsequently discuss.

3.1. Bulk thermodynamics and elastic free energy

Near bulk fluid–solid coexistence, an expansion of the energy around coexistence yields both the bulk thermodynamics and the elastic energy. We assume that the adjacent crystalline layers pick up exactly the structure of the wall pattern and exhibit no spontaneous shearing. This causes a strain ϵ if the wall pattern is incommensurate with the coexisting bulk crystal [37], which in turn gives rise to a free-energy penalty due to the wall-induced elastic distortion of the solid. Harmonic elasticity theory can be used to calculate the penalty Σ_1 from an expansion of the grand potential per area around the coexisting bulk crystal:

$$\Sigma_1/\ell = f_s(\rho_s) + f'_s(\rho_s)(\rho - \rho_s) + \frac{C_{11}}{2}(\epsilon_x^2 + \epsilon_y^2 + \epsilon_z^2) + C_{12}(\epsilon_x\epsilon_y + \epsilon_y\epsilon_z + \epsilon_z\epsilon_x) - \mu\rho + P \quad (7)$$

where ρ is the mean density of the solid which has to be minimized, μ is the given chemical potential, P is the bulk equilibrium fluid pressure, $f_s(\rho)$ is the Helmholtz free energy per volume of the solid, $\epsilon_x, \epsilon_y, \epsilon_z$ are the relative strains in directions x, y, z and C_{ij} are the bulk elastic constants of the fcc solid at coexistence. For a hard-sphere fcc crystal these elastic constants have been determined by computer simulation [38]. As the density is directly dependent on the elastic distortions we can write $\rho = \rho_s(1 - \epsilon_x - \epsilon_y - \epsilon_z)$ and take ϵ_z rather than ρ as the variation parameter with ϵ_x and ϵ_y fixed by the wall pattern. Furthermore, we use the relations

$$\mu_c = \left. \frac{\partial f_s(\rho)}{\partial \rho} \right|_{\rho=\rho_s} = f'_s(\rho_s) \quad P_c = -f_s(\rho_s) + \mu_c \rho_s$$

with μ_c, P_c denoting the chemical potential and the bulk pressure at coexistence. Defining $\Delta P = P_c - P > 0$ and $\Delta\mu = \mu_c - \mu$ we obtain

$$\Sigma_1/\ell = -\Delta P + \Delta\mu \rho_s - \Delta\mu \rho_s(\epsilon_x + \epsilon_y + \epsilon_z) + \frac{C_{11}}{2}(\epsilon_x^2 + \epsilon_y^2 + \epsilon_z^2) + C_{12}(\epsilon_x\epsilon_y + \epsilon_y\epsilon_z + \epsilon_z\epsilon_x). \quad (8)$$

Minimizing with respect to ϵ_z yields $\epsilon_z = \Delta\mu \rho_s / C_{11} - (\epsilon_x + \epsilon_y)C_{12} / C_{11}$. Inserting this into equation (8), the bulk thermodynamics and elastic energy contribution becomes

$$\begin{aligned} \Sigma_1/\ell = & -\Delta P + \mu\rho_s - (\epsilon_x + \epsilon_y) \Delta\mu \rho_s \frac{C_{11} - C_{12}}{C_{11}} \\ & + (\epsilon_x^2 + \epsilon_y^2) \frac{C_{11}^2 - C_{12}^2}{2C_{11}} + \epsilon_x\epsilon_y \frac{C_{12}C_{11} - C_{12}^2}{C_{11}} - \frac{(\Delta\mu \rho_s)^2}{2C_{11}}. \end{aligned} \quad (9)$$

Using thermodynamical relations and the hard-sphere equation of state, we can approximate equation (9) to second order in $\epsilon_x^2, \epsilon_y^2$ and $(\Delta P)^2$. We introduce the density ratio $\tau = \rho_s/\rho_f = 1.103$ and $\alpha = 1 - \tau = 0.103$, the relative density jump across bulk freezing. From the Carnahan–Starling hard-sphere equation of state [39], we obtain

$$\kappa = \rho_f^{-1} \left/ \frac{\partial P}{\partial \rho} \right|_{\rho=\rho_f} = 0.020\sigma^3/(k_B T).$$

Using these abbreviations, we can substitute $\Delta\mu$ via ΔP as $\Delta\mu = \Delta P \tau/\rho_s + (\Delta P)^2 \tau\kappa/\rho_s$. This can be inserted into equation (9) and yields terms of second order.

For the rhombic case, with $\epsilon_x = \epsilon/\sqrt{2}, \epsilon_y = -\epsilon/\sqrt{2}$ we obtain using this procedure

$$\Sigma_1 = \alpha \Delta P \ell + \left(\kappa - \frac{\tau^2}{2C_{11}} \right) (\Delta P)^2 \ell + \beta_r \epsilon^2 \ell + O(\epsilon^3, \epsilon^2 \Delta P, \epsilon (\Delta P)^2, (\Delta P)^3) \quad (10)$$

where $\beta_r = (C_{11} - C_{12})/2 = 24.43k_B T/\sigma^3$.

For the lattice constant mismatch case, on the other hand, we use $\epsilon_x = \epsilon/\sqrt{2}, \epsilon_y = \epsilon/\sqrt{2}$ and insert it into equation (9). This yields

$$\begin{aligned} \Sigma_1 = \alpha \Delta P \ell + \left(\kappa - \frac{\tau^2}{2C_{11}} \right) (\Delta P)^2 \ell + \beta_m \epsilon^2 \ell - \tau \beta^* \Delta P \epsilon \ell \\ + O(\epsilon^3, \epsilon^2 \Delta P, \epsilon (\Delta P)^2, (\Delta P)^3) \end{aligned} \quad (11)$$

with the coefficients

$$\beta_m = (C_{11} + C_{12} - 2C_{12}^2/C_{11})/2 = 38.23k_B T/\sigma^3$$

and

$$\beta^* = \sqrt{2}(C_{11} - C_{12})/C_{11} = 1.03.$$

Note that there is a mixed term proportional to $\Delta P \epsilon$ which vanishes for the rhombic case due to area conservation.

3.2. Surface thermodynamics

The next leading thermodynamic term in an expansion for large ℓ involves interfacial free energies:

$$\Sigma_2 = \gamma_{ws} + \gamma_{sf} - \gamma_{wf}. \quad (12)$$

Here, three interfacial free energies extrapolated to coexistence occur: these are tensions between the patterned wall and the solid (γ_{ws}), between the patterned wall and the fluid (γ_{wf}) and between the bulk solid and the fluid (γ_{sf}). A necessary condition for complete wetting to occur is

$$\gamma_{ws} + \gamma_{sf} \geq \gamma_{wf}. \quad (13)$$

Note that in our calculation we use *extrapolated* interfacial free energies and therefore equation (13) is an extension of Antonow's rule to an inequality. We remark that γ_{ws} and γ_{wf} depend on the wall pattern while γ_{sf} only depends on the relative orientation of the planar solid surface with respect to the fluid. The latter quantity has recently been calculated for hard spheres by computer simulation for different orientations [40] while the first two quantities are not known in general.

3.3. Effective interface potential

The next leading contribution is the effective interface interaction Σ_3 between the wall–solid and the solid–fluid interface as a function of their average distance ℓ . This quantity can be derived from microscopic density functional theory by minimizing the functional with respect to a constraint of fixed width ℓ [41].

For large widths ℓ , as we are dealing with short-ranged interparticle interactions, the asymptotic behaviour of $\Sigma_3(\ell)$ is

$$\Sigma_3 = \gamma_0 e^{-\ell/\ell_0} \quad (14)$$

where γ_0 is a positive prefactor implying that the interaction is repulsive and ℓ_0 is a correlation length in the bulk solid at fluid coexistence.

More subtle information is contained in $\Sigma_3(\ell)$ for smaller ℓ . First, if $\Sigma_3(\ell)$ is monotonically decreasing with ℓ there is complete wetting provided that the relation (13) is fulfilled. Second, non-monotonic behaviour with a minimum of $\Sigma_3(\ell)$ at $\ell = \ell^*$ leads to incomplete wetting with a finite width of ℓ^* at coexistence. Finally, if $\Sigma_3(\ell)$ exhibits oscillations on the scale of the molecular layer widths, wetting may proceed via a finite or infinite cascade of layering transitions [42, 43].

3.4. Prediction of scaling laws

In summary, our theory works for small ΔP , small ϵ and large ℓ . We further assume that the parameters γ_0 and ℓ_0 characterizing the asymptotic form of the effective interface potential $\Sigma_3(\ell)$ are not affected by the small distortion ϵ . We further note that the phenomenological approach does not predict whether complete wetting occurs as it does not fix the sign of $\gamma_{ws} + \gamma_{sf} - \gamma_{wf}$. This requires a full microscopic calculation. However, putting equations (6)–(14) together and minimizing Σ with respect to ℓ , one finds the following quite general scaling relations which no longer depend on the interfacial free energies γ_{ws} , γ_{sf} and γ_{wf} ; the asymptotic relations are valid close to coexistence:

- (i) For vanishing ϵ , the thickness ℓ diverges logarithmically with ΔP :

$$\ell = -\ell_0 \ln \left(\frac{\ell_0 \alpha \Delta P}{\gamma_0} \right) \quad (15)$$

provided that there is complete wetting.

- (ii) Again we are assuming that there is complete wetting for $\epsilon = 0$. Then, for $\epsilon \neq 0$, there is incomplete wetting and the *maximal* thickness which is achieved at $\Delta P = 0$ varies logarithmically with ϵ :

$$\ell = -\ell_0 \ln \left(\frac{\beta \ell_0 \epsilon^2}{\gamma_0} \right) \quad (16)$$

with $\beta = \beta_r$ or $\beta = \beta_m$.

- (iii) For an area-conserving (e.g. rhombic) case: if there are layering transitions, these transitions occur when

$$\alpha \Delta P = \frac{\gamma_0}{\ell_0} e^{-na_z/\ell_0} - \beta_r \epsilon^2 \quad (17)$$

where a_z is the layer spacing in the z -direction. In detail, $a_z = \sqrt{2/3}a_\Delta$ for a triangular wall pattern and $a_z = \sqrt{2}/2a_\Delta$ for a square wall pattern. Equation (17) shows that in the plane spanned by ΔP and ϵ^2 , the transition lines are linear. The slope is predicted to be the very general ratio α/β_r which can be tested against simulations. Note that a linear relation with a slope α/β_r is valid both for wetting and incomplete wetting at $\epsilon = 0$.

- (iv) For a stretched or shrunken lattice the precrystallization of the n th layer at fixed ΔP at a distortion ϵ is determined by the quadratic form

$$\alpha \Delta P - \tau \Delta P \epsilon = \frac{\gamma_0}{\ell_0} e^{-n\alpha z/\ell_0} - \beta_m \epsilon^2. \quad (18)$$

Equation (18) shows that in the plane spanned by ΔP and ϵ , the transition lines are parabolic, with their apices lying on the straight line $\epsilon(\Delta P) = [\beta^*/(2\beta_m)] \Delta P$. The lowest possible prefreezing pressure is

$$\Delta P_{\min} = \frac{2\beta_m \alpha - 2\sqrt{\beta_m^2 \alpha^2 + (\beta^*)^2 \beta_m \alpha \Delta P_n}}{(\beta^*)^2} \quad (19)$$

with ΔP_n being the prefreezing pressure of the undistorted n th layer as obtained by inverting equation (15) or by computer simulations. Note the interesting fact that a slightly expanded lattice will have a *lower* prefreezing pressure than the ideal matching lattice. However, it will not show complete wetting.

4. Simulation technique

We simulate the hard-sphere fluid using a rectangular simulation box of size $V = L_x L_y L_z$ with periodic boundary conditions in the x - and y -directions. In the z -direction the system is confined by two patterned walls at distance L_z . The surface area of the simulation box under consideration is $A = L_x L_y$. Onto these walls any pattern can be imprinted as described in section 2.

We use standard NVT Monte Carlo (MC) simulation techniques [35, 44–46]. In NVT simulations, the volume, the (irrelevant) temperature and the particle number of the system are fixed. To check that the results are independent of the ensemble used, we also perform some $NP_z T$ Monte Carlo simulations. In this case the walls in the z -direction can fluctuate under an external applied pressure P_z . Yet most results have been achieved by NVT simulations as they have the advantage of better equilibration. Especially with crystalline layers present, $NP_z T$ simulations equilibrate only very slowly. Within the statistical uncertainties, the two set-ups yield the same results.

Furthermore, the size of the system in the z -direction, i.e. perpendicular to the wall, has to be fairly large to avoid capillary effects and other spurious mutual influences of the two walls. Moreover, we need large surface areas to exclude effects from the lateral periodic boundary conditions. System sizes of about $N = 640$ to $N = 10\,400$ particles yielding surface areas of about $A = 16\sigma^2$ to $A = 271\sigma^2$ and an extension into the z -direction of about $L_z = 40\sigma$ to $L_z = 100\sigma$ have been used during our simulations. In order to avoid lateral compressional strains in the crystal, the lengths L_x and L_y were adjusted to the given crystallographic orientation such that a laterally periodic bulk crystal fits exactly into the simulation box.

In figure 3 we show a typical snapshot of a computer simulation, where a hard-sphere fluid is in contact with a triangular wall pattern. The system shows the prefreezing of the first few layers and inherits the offered triangular wall pattern.

5. Order parameters

To detect layerwise precrystallization we monitored suitable order parameters during our simulations. To analyse in particular the behaviour of freezing in a sequence of layers we

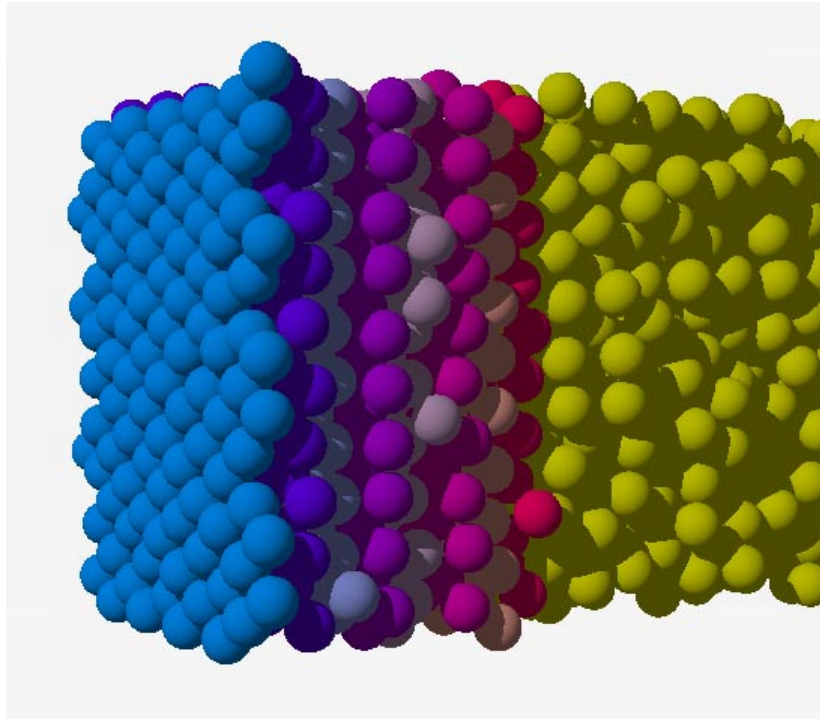


Figure 3. A snapshot at $\eta = 0.490$ and $P^* = 11.25$ for a triangular wall. The first few layers are marked with different shadings to show their frozen nature (left) while toward the bulk (right) the system becomes fully fluid. On the front area of the first layer the system mimics the triangular wall pattern which is not shown for the sake of clarity.

(This figure is in colour only in the electronic version, see www.iop.org)

first have to determine the position of the minima in the laterally integrated density profile $\rho(z)$ defined via

$$\rho(z) = \int_{-\infty}^{\infty} dx \int_{-\infty}^{\infty} dy \rho(x, y, z) \quad (20)$$

where $\rho(x, y, z)$ is the full inhomogeneous one-particle density field.

The minima of $\rho(z)$ define the spacing of the n th layers in the z -direction. The analysis of an order parameter in the n th layer can be performed for each layer, i.e. for all particles in a chosen layer.

In the following we describe four different order parameters which were used as diagnostics for the freezing transition. In general we find consistency between these different diagnostics.

5.1. Bond order parameter

One basic order parameter for detecting precrystallization is a bond-order parameter as frequently used in 2D hard-disc systems [47, 48]. These bond-orientational order parameters detect the symmetry of the ‘bonds’ between particles. For the sixfold symmetry of the triangular pattern, the $\Psi^{(6)}$ parameter is used and for the fourfold symmetry of the square pattern $\Psi^{(4)}$ is used. For linear ordered systems such as those given by the fcc (110) and hcp (110) wall, the $\Psi^{(2)}$ order parameter is applied.

In general the order parameter $\Psi_n^{(k)}$ for k -fold symmetry in the n th layer is defined as

$$\Psi_n^{(k)} = \left\langle \left| \frac{1}{N_l} \sum_{i=1}^{N_l} \sum_{j=1}^{N_i} e^{ki\theta_{ij}} \right| \right\rangle \quad (21)$$

where θ_{ij} is the angle between the separation vector of the particles i and j and an arbitrary but fixed reference axis. The sum i is over all particles of the n th layer and the sum j is over the N_i neighbours of particle i in the same layer. For simulation purposes particles are defined as neighbours if the distance between particle i and j is less than $(1.35-1.40)\sigma$. This somewhat arbitrary definition for neighbours can be used as the resulting $\Psi_n^{(k)}$ depends only weakly on the exact definition of a neighbour distance.

An example of an order parameter distribution in the different layers for $k = 4$ is shown in figure 4. The distribution clearly signals whether the layer has fluidlike or solidlike bond-orientational order: The first layer shows a very pronounced fourfold symmetry. The second layer is still well ordered but the ordering is less pronounced. The third layer is just at the transition to the ordered fourfold symmetry and all other layers are fluidlike.

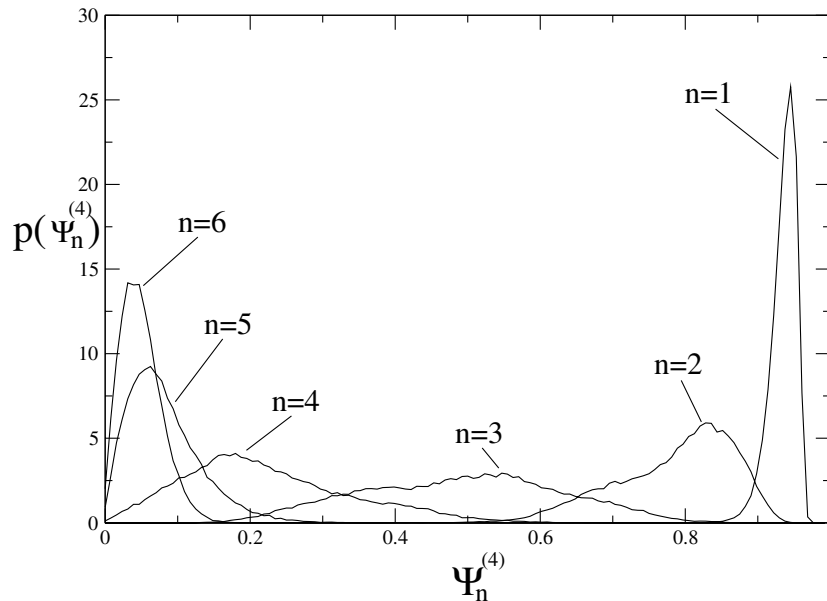


Figure 4. The order parameter distribution $P(\Psi_n^{(4)})$ for the first six layers of a hard-sphere fluid near a square-patterned wall with fourfold symmetry at $\eta = 0.488$ and $P^* = 11.06$.

5.2. Stacking order parameter

A crystal on top of a triangular or rhombic wall pattern can have different stacking orders. If the wall has the fixed stacking A, the next layer is either packed in B or C and the following one can then be either A or C, or A or B, depending on the second one. This can be exploited to define a stacking order parameter Φ_n , which probes the ideality of stacking in the n th layer and is sensitive to layerwise precrystallization.

In what follows, we explain the definition of Φ_n for a triangular pattern, the generalization to a rhombic pattern being straightforward.

For each layer n the stacking properties are probed by projecting the particle positions onto the surface. Figure 1 depicts the honeycomb-like cells A, B and C which correspond to the three stacking possibilities that the projection can fall into. Hence one obtains the averaged probabilities $\{p_n^{(A)}, p_n^{(B)}, p_n^{(C)}\}$ for a particle in the n th layer to be projected into a honeycomb of type A, B or C. The stacking order parameter Φ_n for the n th layer is now defined as the difference between the two largest numbers of the set $\{p_n^{(A)}, p_n^{(B)}, p_n^{(C)}\}$. For a fluid near a non-structured wall, all stacking probabilities are equal; hence Φ_n vanishes. For the first layer of a structured wall, an inhomogeneous liquid has $p_1^{(A)} < p_1^{(B)}$, as it is unlikely that a particle will sit on top of a fixed wall sphere. Furthermore, due to symmetry, $p_1^{(B)} = p_1^{(C)}$; therefore Φ_1 vanishes again. A freezing transition in the n th layer is indicated when $\Phi_n > 0$, corresponding to a broken *discrete* symmetry of the two stacking possibilities. Finally, in a perfect solid with close-packing density, $\Phi_n = 1$.

The order parameter Φ_n has the important property that it is zero for the inhomogeneous fluid phase but non-zero for a crystalline layer. Hence it yields precise information about precrystallization. Figure 5 shows an example of the order parameters of the first four layers for a triangular wall as functions of the bulk pressure, proving that Φ_n provides a sharp diagnostic for precrystallization.

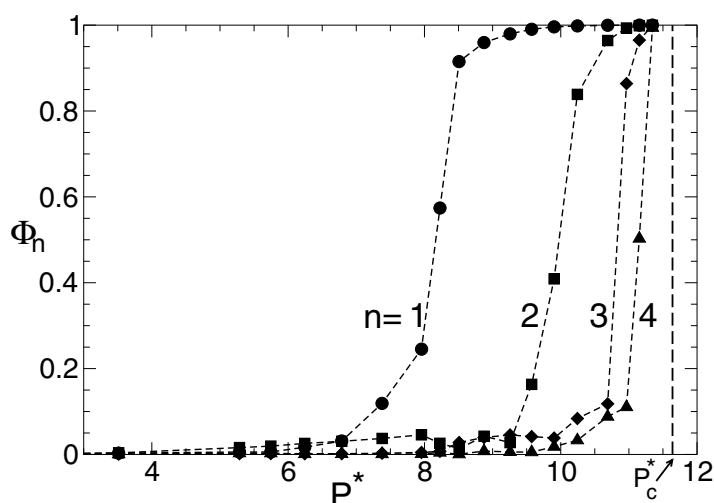


Figure 5. Order parameter Φ_n ($n = 1, 2, 3, 4$) versus reduced pressure P^* for a triangular wall pattern with P_c^* indicating the coexistence pressure of the bulk system. The system size is $L_z/\sigma = 45$ and $A^* = 106$.

5.3. Minima of the density profile

Another possibility for checking the freezing of the system is to analyse the depth of the minima of the lateral integrated density profile as given by equation (20). We find that the precrystallization can be detected by a rough criterion. It occurs if the minimal density drops to about 5% of the corresponding bulk density. This criterion is in accordance with the diagnostics using the other order parameters and has the additional advantage that it is robust close to coexistence. In figure 6 an example of $\rho(z)$ is shown. The freezing of the first two layers can be clearly seen from a very small density minimum. The third layer is about to freeze, consistent with the diagnostics of the order parameters Φ_n and $\Psi_n^{(6)}$.

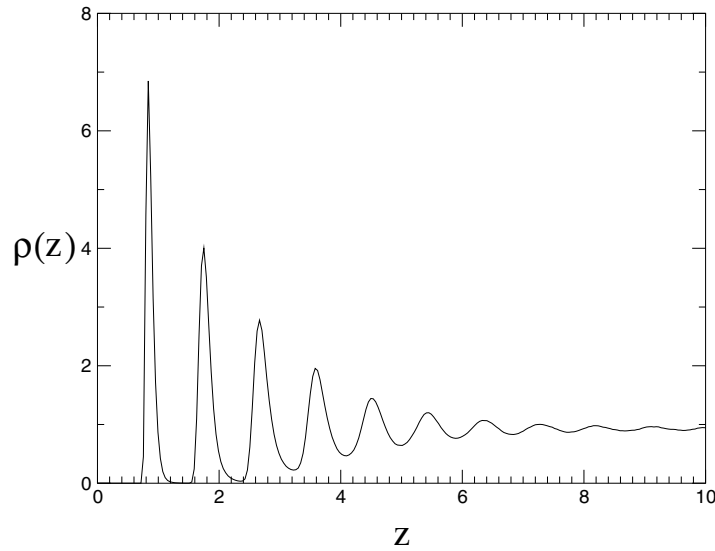


Figure 6. The density profile of the hard-sphere fluid at a pressure of $P^* = 10.87$ near to a structured wall with a triangular pattern imprinted.

5.4. Lindemann parameter

Another order parameter which has proven to be useful as regards the freezing of a bulk solid is the Lindemann parameter [49]. The normalized root mean square displacement of particles around their ideal lattice positions \vec{r}_i^w

$$L := \frac{\sqrt{\langle (\vec{r}_i - \vec{r}_i^w)^2 \rangle}}{a} \quad (22)$$

is known as the Lindemann parameter L of the solid [50].

The traditional Lindemann melting rule [49] states that a bulk solid melts if L is roughly 10%. We check this rule for interfacial freezing. In order to do so, we define a layer-resolved Lindemann parameter L_n by applying equation (22) to all particles in the n th layer. Simulation data for L_n are shown in figure 7 for the first four layers of a triangular wall pattern. First, it can be seen that L_n varies very slowly with the pressure, thus not providing a sharp diagnostic for interfacial freezing. If the interfacial freezing is fixed by the clear-cut diagnostics of Φ_n (see figure 5), however, then one can check how large L_n is at interfacial melting. Indeed L_n at melting varies from 0.18 for the first layer to 0.14 for the fourth layer but is close to the bulk value of 0.13 [49] as presented by the dashed line in figure 7. This implies that the rough Lindemann melting rule also applies for interfacial freezing. We have further tested the Lindemann rule for other wall structures and find similar behaviour.

6. Analysis for finite system size

Particular attention has to be paid to finite-size effects in the system under consideration. In the length in the z -direction as well as in the area $A = L_x L_y$, finite-size effects could affect the results. We use the system with the commensurate triangular wall pattern to investigate these finite-size effects in more detail.

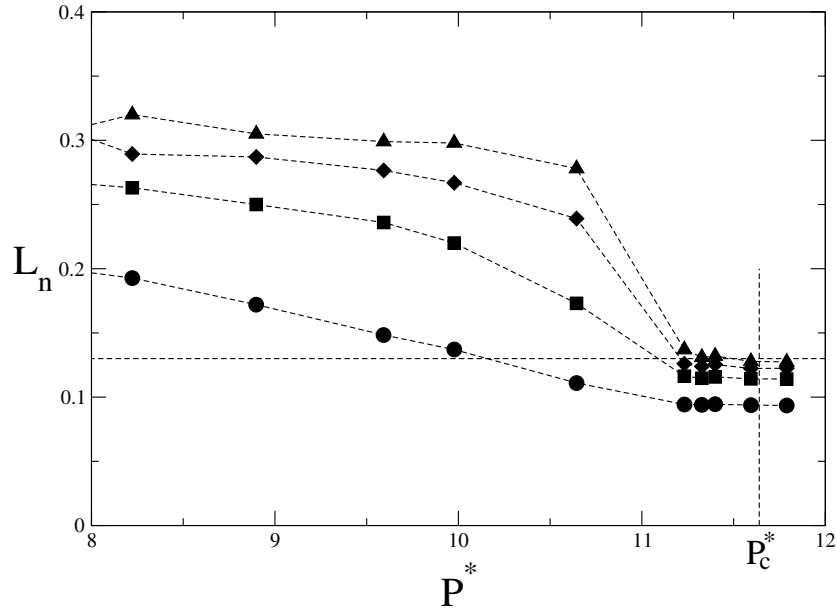


Figure 7. The Lindemann parameter L_n for the first four layers (from bottom to top) for a triangular wall pattern. The horizontal dashed line indicates the bulk freezing Lindemann parameter and the vertical dashed line indicates the bulk freezing pressure P_c^* .

From reference [51] we know that box lengths of $L_z > 40\sigma$ are necessary to avoid finite-size effects such as capillary condensation. We check our simulation results therefore with different box lengths ranging from $L_z = 40\sigma$ to $L_z = 100\sigma$. In this analysis we could not find any dependence on the box length and hence can confirm the results of [51, 52]. We conclude that we are beyond capillary effects [52] and other effects related to a finite box length.

Even more important is the finite-size effect of the surface area A . Hence we made a careful analysis of surface areas between $A = L_x L_y = 16\sigma^2$ and $A = L_x L_y = 271\sigma^2$. We find a size dependency for small surface areas, as depicted in figure 8. Only around $100\sigma^2$ do the curves begin to approach asymptotic values. Explicit data for this are collected in table 1. We also extract the average value for the freezing densities for the triangular wall from the data of figure 8 and table 1 for values of $A > 100\sigma^2$. This gives rise to the statistical errors which are also presented in the table.

Table 1. Freezing pressures P^* for the first four layers of a triangular wall pattern for various surface areas A . The average is formed from the data for $A > 100\sigma^2$, which do not exhibit finite-size effects any longer.

A/σ^2	Layer 1	Layer 2	Layer 3	Layer 4
17.0	9.84	11.06	10.96	11.25
38.2	9.30	10.87	10.93	10.96
67.9	8.71	10.70	10.93	11.20
106.2	8.53	10.60	11.10	11.28
152.9	8.52	10.53	11.08	11.15
271.9	8.51	10.40	10.97	11.15
Average	8.53 ± 0.13	10.51 ± 0.12	11.05 ± 0.11	11.20 ± 0.05

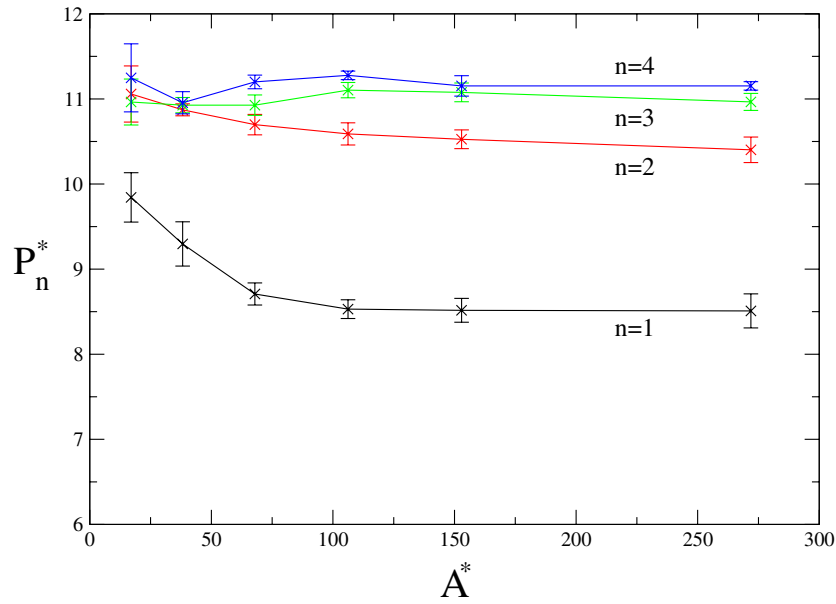


Figure 8. The transition pressure P_n^* in different layers $n = 1, 2, 3, 4$ versus surface area for a triangular wall pattern. The pressure saturates for all layers at about $A \approx 100\sigma^2$.

From the finite-size analysis in the z -direction and area A we find that systems of around $L_z = 45\sigma$ and areas of $106\sigma^2$ are sufficient. Our further studies are based on systems with such a size.

7. Results

7.1. Triangular (fcc (111)) and rhombic wall patterns

The most favourable wall pattern which we can offer for the system is a triangular pattern with a lattice spacing which exactly matches the bulk crystal at bulk melting [33, 51]. We use this configuration as a reference point for the investigation of wall patterns.

Performing simulations on such systems yields complete wetting by crystalline layers starting at very low bulk pressures of $P^* = 8.53$ (corresponding to a packing fraction of $\eta = 0.457$) well below bulk freezing. From this pressure onwards we find a cascade of layered freezing transitions whose pressures are summarized in table 1.

The fact that the wetting proceeds layer by layer is a subtle effect. For instance, in sedimentation profiles [53] the opposite, namely a continuous growth, as a function of the gravitational constant was found. The layerwise freezing transitions in our system can be understood intuitively as follows: when the first layer freezes at the pressure P_1^* , the spheres become much more localized, reflecting the triangular pattern. These frozen layers then act as a template for freezing of the second layer at P_2^* . P_2^* is larger than P_1^* , as the spheres in the first layer are still mobile. This is repeated for the third layer and so on, forming a whole cascade of layering transitions.

As predicted by asymptotic theory, complete wetting is achieved by a logarithmic growth of the wetting layer $\ell \propto -\ln \Delta P^*$ as shown in figure 9. Here we show the prefreezing as found with the order parameter Φ_n . Except for the first layer, which is not expected to follow

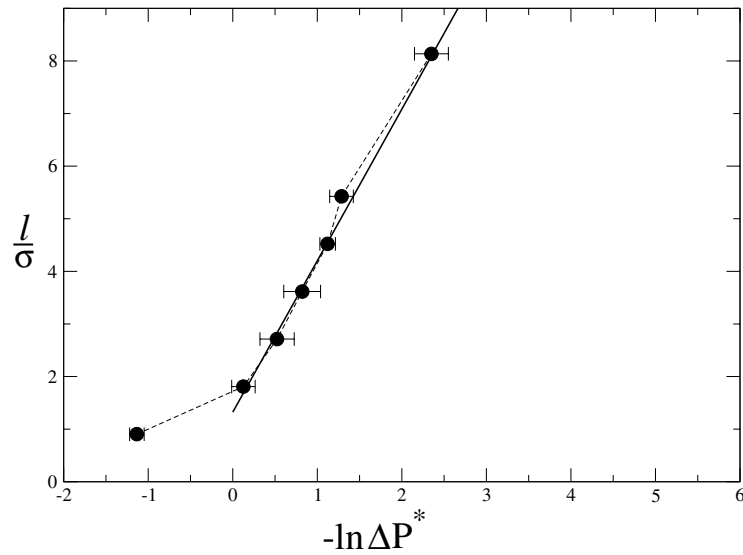


Figure 9. The thickness of the crystalline wetting layer ℓ versus $-\ln \Delta P^*$ as measured by the order parameters Φ_n . The straight line is the best linear fit to the data excluding the first layer.

a logarithmic growth law as the theory is only valid for large ℓ , we find a good agreement with a logarithmic growth of the wetting layer. Although we only have data for a limited range of layer thicknesses as shown in figure 9, the fact that the logarithmic growth law is fulfilled very well gives strong evidence that the wetting is really complete, i.e. every layer is frozen for $P \rightarrow P_c$.

From a fit of the data from figure 9 we can extract the two parameters γ_0 and ℓ_0 which we used in the phenomenological theory; see equation (14). The actual value for the correlation length is $\ell_0 = 2.50\sigma$ and the amplitude¹ is $\gamma_0 = 0.47k_B T/\sigma^2$.

We now distort the triangular wall pattern to create a rhombic pattern with $\epsilon > 0$; see equation (3). The maximal distortion is given for two spheres touching and occurs at $\epsilon^2 \rightarrow \epsilon_m^2 \equiv 0.021$. At this point the cost in free energy due to the lateral distortion diverges. As the theory considers only harmonic distortions, any higher-order effects and especially this divergence are not accounted for. Computer simulations prove this behaviour. We obtain for a rhombic distortion again a wetting by a cascade of crystalline layers but at shifted freezing pressure. The actual data are collected in table 2.

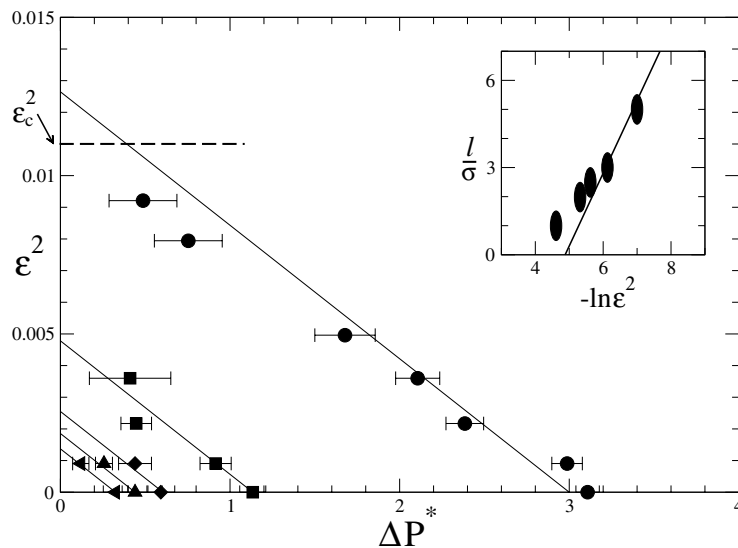
Putting the parameters γ_0 and ℓ_0 into equation (16) and equation (17) we can verify the two other theoretical predictions. We show the results in figure 10. The inset of figure 10 shows our simulation data using a log-linear plot for equation (16) where we do indeed find qualitative agreement. However, the uncertainty of the data is large since the measured thickness of the layer is actually a multiple of the layer spacing $a_z = \sqrt{2/3}a_\Delta$ in the z -direction. Note that the solid line in the inset of figure 10 involves no fit parameters as these are fixed by the fit as shown in figure 9.

Furthermore, the layering transition of the n th layer can be estimated by the theory to occur according to equation (17). In the plane spanned by ΔP and ϵ^2 , these transition lines are predicted to be linear. In fact, as shown in figure 10, most of our computer simulation data for

¹ In comparison to those of [33], the fitting parameters that we get are slightly different, as we fit the data only for the asymptotic part.

Table 2. Prefreezing pressures P^* of the first five layers for a triangular wall pattern which is distorted to a rhombic one by a distortion ϵ^2 .

ϵ^2	a/σ	Layer 1	Layer 2	Layer 3	Layer 4	Layer 5
0.0	1.108	8.53	10.51	11.05	11.20	11.32
0.0009	1.063	8.65	10.73	11.20	11.38	11.52
0.0022	1.072	9.26	11.19	11.64	—	—
0.0036	1.085	9.53	11.23	—	—	—
0.0050	1.054	9.96	11.64	—	—	—
0.0079	1.040	10.89	—	—	—	—
0.0092	1.035	11.15	—	—	—	—
0.0115	1.027	—	—	—	—	—
0.0143	1.018	—	—	—	—	—
0.0190	1.005	—	—	—	—	—

**Figure 10.** The location of the first five layering transitions in the plane spanned by ΔP^* and ϵ^2 . The symbols represent simulation data with their statistical errors. The straight lines are the theoretical predictions. The simulation result for ϵ_c^2 is indicated by the dashed line. The inset shows the maximal thickness ℓ versus $-\ln \epsilon^2$. The straight line is the theoretical prediction; see equation (17). Symbols represent simulation data with the sizes of the symbols indicating the error.

the layering transitions fall upon straight lines. We emphasize that the slope does not involve any fit parameter; therefore quantitative agreement between theory and simulation is obtained within the error bars of the simulation data.

However, there are deviations for large strains which we attribute to anharmonic elasticity. In fact, when $\epsilon^2 \rightarrow \epsilon_m^2 \equiv 0.021$, the divergence in free energy is not accounted for in the theory. Furthermore, the logarithmic growth law does not hold for the very first layer as it is derived asymptotically only for large ℓ . As we did not include the data for the first layer into the linear fit, this leads us to adjust the offset of the theoretical lines in figure 10 for the first two layers to the actual measured data from the computer simulation. However, the slope of these lines is still in agreement with the theory, as the theory is quite robust against the exact form of the effective interface potential $\Sigma_3(\ell)$. We emphasize that none of the other layers require any

additional fit parameter. The slope and offset are given by the theoretical prediction of the phenomenological theory.

A further notable fact drawn from figure 10 is that there is no precrystallization at all if ϵ exceeds a critical value ϵ_c . The theory predicts $\epsilon_c^2 = 0.014$ while the simulations yield a smaller value, $\epsilon_c^2 = 0.011 \pm 0.001$ due to the anharmonic elastic free energy. For $\epsilon_c^2 < \epsilon^2 < \epsilon_m^2 = 0.021$ the large free-energy cost of elastic distortion prevents the system from undergoing precrystallization. The actual situation is a strongly inhomogeneous fluid, reflecting the surface pattern which remains stable up to the bulk freezing point.

As discussed within the framework of the phenomenological wetting theory, we investigated the effect of a lattice constant mismatch for the triangular lattice. This results in a growing or shrinking of the wall pattern compared to the ideal one. In figure 11 we plot the theoretical prediction of the resulting prefreezing pressures versus the distortion ϵ —see equation (4) and equation (11)—and compare it with the computer simulation data. There is a good agreement between the computer simulation data and the theoretical prediction. For the first layer, there are deviations which we attribute to the non-quadratic corrections in the thermodynamical part of the theory.

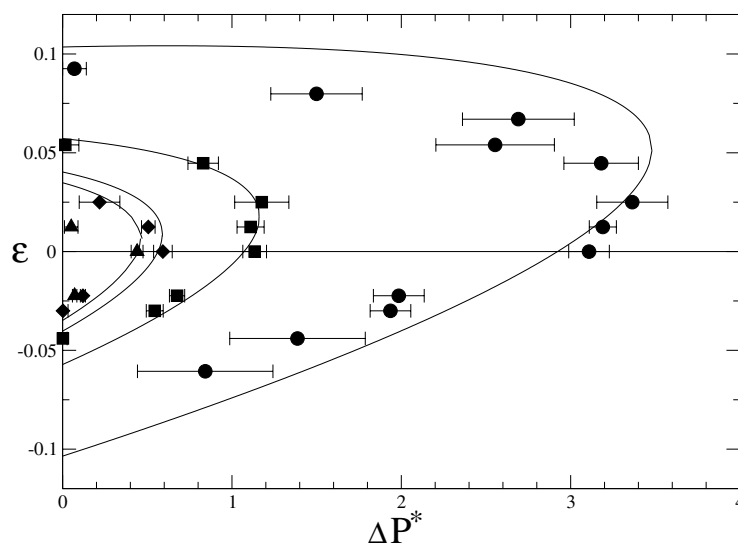


Figure 11. The location of the first four layering transitions in the plane spanned by ΔP^* and ϵ . The curves are the theoretical predictions for a crystal lattice constant which is shrunk ($\epsilon < 0$) or expanded ($\epsilon > 0$) compared to that of the coexisting bulk crystal. The different symbols show computer simulation results for the crystallization transitions in the different layers with their error bars.

For $\epsilon = 0$ there is complete wetting by the crystal. On increasing or decreasing ϵ , a crystalline sheet of prefrozen layers still exists. However, the shrinking or growing of the pattern leads to a shift in the onset of the freezing density as well as to a reduction of the maximal thickness achieved for the wetting layer. No complete wetting is possible any longer. Comparing this situation with the rhombic distortion we find that the onset of prefreezing no longer follows a pure quadratic ϵ^2 -behaviour. The additional expansion or shrinking of the crystal leads to a linear term in $\epsilon \Delta P$ which shifts the wetting curves. For a slightly stretched crystal with $\epsilon > 0$, the pressure for which precrystallization still occurs is now shifted to *lower* values compared to the ideal matching substrate pattern with $\epsilon = 0$. We note though that there is no complete wetting any longer if $\epsilon \neq 0$. The theoretical critical distortion above which

there is no precrystallization at all is $\epsilon_c = 0.10$. There is no maximal distortion for an enlarged lattice and a maximal distortion of $|\epsilon_m| = 0.14$ for a shrunken lattice. The lowest possible prefreezing pressure is $P^* = 8.16$ as predicted by the theory and $P^* = 8.28 \pm 0.21$ as found in the computer simulations.

7.2. Hard-sphere fluid near a fcc (100) wall

We continue the analysis with a square wall pattern which is a cut through a (100) plane of a fcc crystal as shown in figure 2(b). In contrast to the results for the triangular wall, we do not find complete wetting in this case—not even for the ideal lattice spacing. This can be concluded from figure 12 where the growth of the wetting layer seems to saturate at around $\ell_m = 3.9\sigma$ leading to incomplete wetting by the crystal. However, approaching coexistence further poses enormous equilibration problems in the simulations. However, the decreasing slope in the ℓ/σ versus $-\ln \Delta P^*$ plot seems to indicate incomplete wetting.

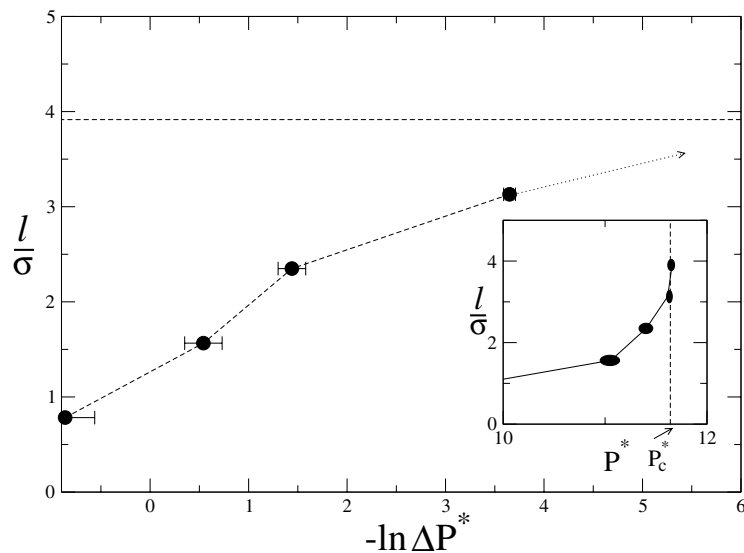


Figure 12. Thickness ℓ of the wetting layer versus $-\ln \Delta P^*$, as measured using the order parameters $\Psi_n^{(4)}$. The thickness seems to converge toward 3.9σ as shown in the inset, where the thickness ℓ is plotted versus P^* .

As discussed within the framework of the phenomenological wetting theory, we also investigated the effect of a lattice constant mismatch for the square lattice. This results in a growing or shrinking of the wall pattern compared to the ideal one.

In figure 13, the theoretical prediction and computer simulation data for the resulting prefreezing pressures versus the distortion ϵ are plotted; see equation (5) and equation (11). We start at $\epsilon = 0$ with the prefreezing pressures as found in the computer simulation and shown in figure 12 and extend these points with the data as obtained from equation (17).

For $\epsilon = 0$ we have incomplete wetting by a few prefrozen layers. On increasing ϵ , a crystalline sheet of prefrozen layers still exists. However, the shrinking or growing of the pattern leads to a shift in the onset of the freezing density as well as to a reduction of the maximal thickness achieved for the wetting layer similar to the one detected for the triangular lattice. In fact, the theoretical critical distortion is $\epsilon_c = 0.09$ while there is no maximal distortion for an expanded lattice and a maximal distortion of $|\epsilon_m| = 0.14$ for a shrunken lattice. The

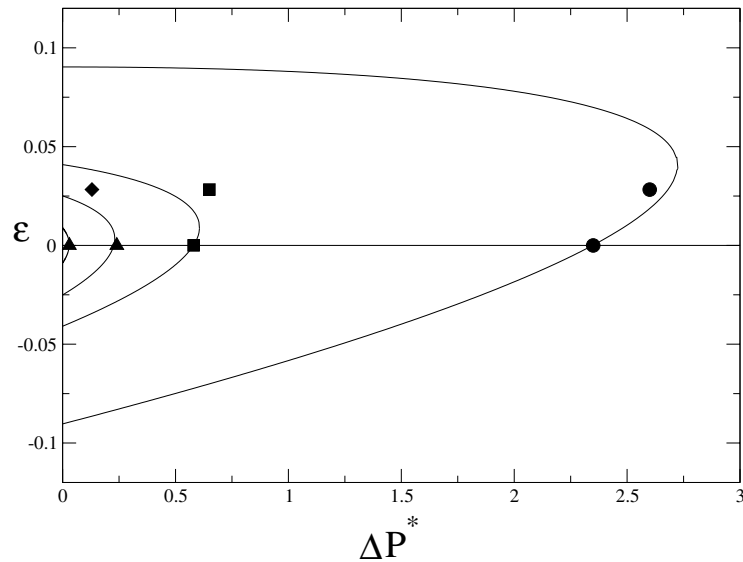


Figure 13. The location of the first four layering transitions in the plane spanned by ΔP^* and ϵ . The curves are the theoretical predictions for a crystal lattice constant which is shrunk ($\epsilon < 0$) or expanded ($\epsilon > 0$) compared to that of the coexisting bulk crystal. The different symbols show computer simulation results for the crystallization transitions in the different layers.

theoretical value for the lowest prefreezing pressure is $P^* = 8.92$, which is higher than that for the corresponding (111) case but lower than the prefreezing pressure of the undistorted (100) crystal.

7.3. Hard-sphere fluid near a fcc (110) wall

We now focus our analysis on a wall pattern which is a cut through the (110) plane of a fcc crystal as shown in figure 2(c). To analyse this system we mainly apply the $\Psi_n^{(2)}$ order parameter (see figure 14). As this order parameter only indicates a one-dimensional ordered system which is not necessarily two-dimensionally ordered, we compare the data with the order parameter as obtained from the minima of the density profile. We find good agreement in locating precrystallization using the two different order parameters.

Like for the square lattice, we find incomplete wetting by the crystal. The crystallization proceeds via discrete layering but stops at $P^* \rightarrow P_c^*$. The width of the wetting layer converges toward a maximum thickness of about $\ell_m = 5.5\sigma$ when approaching the bulk freezing point. Again, the deviation from a logarithmic growth law is small, so there is still some uncertainty in this prediction.

7.4. Hard-sphere fluid near a hcp (110) wall

Using the order parameter $\Psi_n^{(2)}$ for the hcp (110) wall, we find precrystallization starting at very low values of $P^* = 9.5$ leading to complete wetting by the crystal. This wetting behaviour is summarized in figure 15 where we show the thickness of the wetting layer ℓ versus $-\ln \Delta P^*$. Although we were not able to resolve the order parameter to a very high layer thickness, the thickness measured from the minima of the density profile clearly indicates a logarithmic growth of the wetting layer.

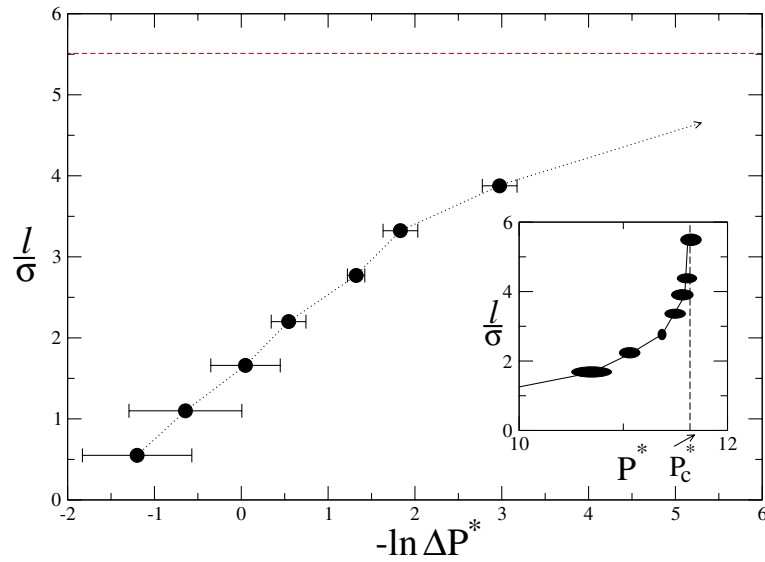


Figure 14. Thickness ℓ of the crystalline wetting layer versus $-\ln \Delta P^*$ as measured using the order parameters $\Psi_n^{(2)}$. The thickness seems to converge toward 5.5σ as shown in the inset, where the thickness ℓ is plotted versus P^* .

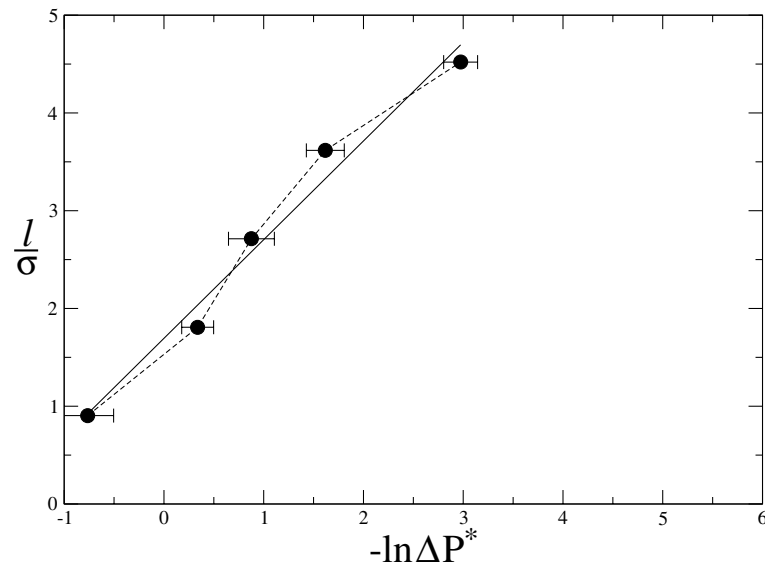


Figure 15. Thickness ℓ of the wetting layer versus $-\ln \Delta P^*$ as measured using the order parameters $\Psi_n^{(2)}$. The straight line is the best linear fit for the simulation data.

Again, complete wetting proceeds via a cascade of discrete layering transitions. From a fit of the data of figure 15 we extract the correlation length of $\ell_0 = 1.01\sigma$ and the amplitude of $\gamma_0 = 0.56k_B T/\sigma^2$. ℓ_0 is remarkably lower than for a triangular pattern. Clearly, ℓ_0 depends on the surface pattern, as described in more detail in the different context of surface melting [54,55].

8. Conclusions

In conclusion, the structure of a substrate pattern profoundly influences the scenario of wetting by crystalline phases. First, the onset of precrystallization can be significantly shifted away from coexistence by using a pattern that favours the crystal. We have investigated different patterns such as the triangular one and the hcp (110) one which lead to complete wetting by crystalline sheets. However, by applying patterns which are distorted from the ideal form such as the rhombic pattern or an ideal pattern which has lattice constant mismatch, we find incomplete wetting by a crystal, i.e. there are only a finite number of crystalline sheets as bulk coexistence is approached. This number depends crucially on the lattice distortion with respect to an ideal lattice, which is commensurate with a coexisting bulk crystal. Yet there is an important fact to note: despite having no complete wetting any longer, it is possible to shift the onset of prefreezing to even lower pressures by slightly expanding the wall pattern compared to the ideal-matching coexisting crystal. Furthermore, even a commensurate wall pattern can lead to incomplete wetting as demonstrated for the square wall and the fcc (110) pattern. In the case of very unfavourable structures, e.g. the highly distorted rhombic pattern, precrystallization is completely prevented. Moreover, we have confirmed the Lindemann melting rule even for interfacial freezing. All of our predictions can be verified by real-space or scattering experiments on sterically stabilized colloidal suspensions near a patterned wall.

We finish with a couple of remarks. First, the fact that a suitable wall pattern can generate sheets of a crystal which is unstable as a pure bulk phase could possibly be exploited for producing colloidal crystals with unconventional structures relevant e.g. for optical band-gap materials. An 'exotic' example is a one-component quasicrystal which may be nucleated at a suitable non-periodic wall pattern. Second, a more subtle question which we did not address in our paper concerns the roughness of the solid–fluid interfaces. This is still an open issue. Third, an as yet unsolved question is the formation of crystal defects at the interface if the wall pattern is too different from the bulk crystal structure. Such effects are much more complicated and are encaptured neither by our simple theory nor by our finite-size simulations. Finally, our ideas in combining thermodynamical and elastic terms in the theory of wetting by a solid phase can also be useful for other problems, e.g. that of triple-point wetting [19]. Furthermore, the precrystallization effects discovered by simulation could provide benchmark data for testing microscopic density functional theories of inhomogeneous hard-sphere freezing as, e.g., given in the Rosenfeld approximation [56]. Our further work will be focused in this direction.

Acknowledgments

We thank M Schmidt, R Evans and A van Blaaderen for helpful discussions. This work was supported by the Deutsche Forschungsgemeinschaft within project LO 418/5 and by the DAAD foundation within the ARC programme.

References

- [1] Dietrich S 1988 *Phase Transitions and Critical Phenomena* vol 12, ed C Domb and J L Lebowitz (London: Academic) pp 1–128
- [2] Evans R 1990 *Liquids at Interfaces (Les Houches Session XLVIII)* ed J Charvolin, J F Joanny and J Zinn-Justin (Amsterdam: Elsevier) p 1ff
- [3] Courtemanche D J and van Swol F 1992 *Phys. Rev. Lett.* **69** 2078
- [4] Courtemanche D J, Pasmore T A and van Swol F 1993 *Mol. Phys.* **80** 861
- [5] Weinstein A and Safran S A 1996 *Phys. Rev. E* **53** R45
- [6] Weinstein A and Safran S A 1998 *Europhys. Lett.* **42** 61

- [7] Tkachenko A V and Rabin Y 1997 *Phys. Rev. E* **55** 778
- [8] Mukherjee P K and Deutsch M 2000 *Phys. Rev. E* **61** 637
- [9] Smith P, Lynden-Bell R M, Earnshaw J C and Smith W 1999 *Mol. Phys.* **96** 249
- [10] Merkl C, Pfohl T and Riegler H 1997 *Phys. Rev. Lett.* **79** 4625
- [11] Pfohl T, Beaglehole D and Riegler H 1996 *Chem. Phys. Lett.* **260** 82
- [12] Earnshaw J C and Hughes C J 1992 *Phys. Rev. A* **46** 4494
- [13] Wu X Z, Sirota E B, Sinha S K, Ocko B M and Deutsch M 1993 *Phys. Rev. Lett.* **70** 958
- [14] Wu X Z, Sirota E B, Sinha S K, Ocko B M and Deutsch M 1995 *Phys. Rev. Lett.* **75** 1332
- [15] Hayami Y and Findenegg G 1997 *Langmuir* **13** 4865
- [16] Maeda N and Yaminsky V V 2000 *Phys. Rev. Lett.* **84** 698
- [17] Gang O, Ocko B M, Wu X Z, Sirota E B and Deutsch M 1998 *Phys. Rev. Lett.* **80** 1264
- [18] Gang O, Ocko B M, Wu X Z, Sirota E B and Deutsch M 1999 *Phys. Rev. Lett.* **82** 588
- [19] Klier J, Weichhard C and Leiderer P 2000 *Physica B* **284** 391
- [20] Lenz P and Lipowsky R 1998 *Phys. Rev. Lett.* **80** 1920
- [21] Bauer C and Dietrich S 1999 *Phys. Rev. E* **60** 6919
- [22] Frink L J and Salingers A G 1999 *J. Chem. Phys.* **110** 5969
- [23] Herminghaus S, Fery A, Schlagowski S, Jacobs K, Seemann R, Gau H, Mönch W and Pompe T 2000 *J. Phys.: Condens. Matter* **12** A57
- [24] van Blaaderen A, Ruel R and Wiltzius P 1997 *Nature* **385** 321
- [25] Mio C and Marr D W M 1999 *Langmuir* **15** 8565
- [26] Chen K M, Jiang X, Kimerling L C and Hammond P T 2000 *Langmuir* **16** 7825
- [27] Lin K, Crocker J C, Prasad V, Schofield A, Weitz D A and Lubensky T C, and Yodh A G 2000 *Phys. Rev. Lett.* **85** 1770
- [28] Arora A K and Rajagopalan R 1997 *Curr. Opin. Colloid Interface Sci.* **2** 391
- [29] Burmeister F, Schäfle C, Matthes T, Böhmisch M, Boneberg J and Leiderer P 1997 *Langmuir* **13** 2983
- [30] Aizenberg J, Braun P V and Wiltzius P 2000 *Phys. Rev. Lett.* **84** 2997
- [31] Shimizu T and Yamamoto T 2000 *J. Chem. Phys.* **113** 3351
- [32] Huisman W J, Peters J F, Zwaneburg M J, de Vries S A, Derry T E, Abernathy D and van der Veen J F 1997 *Nature* **390** 379
- [33] Heni M and Löwen H 2000 *Phys. Rev. Lett.* **85** 3668
- [34] Ree F H and Hoover W G 1967 *J. Chem. Phys.* **46** 4181
- [35] Frenkel D and Smit B 1996 *Understanding Molecular Simulation* (San Diego, CA: Academic)
- [36] van Blaaderen A 2000 private communication
- [37] Gittes F T and Schick M 1984 *Phys. Rev. B* **30** 209
- [38] Frenkel D and Ladd A J C 1987 *Phys. Rev. Lett.* **59** 1169
- [39] Carnahan N F and Starling K E 1969 *J. Chem. Phys.* **51** 635
- [40] Davidchack R L and Laird B B 2000 *Phys. Rev. Lett.* **85** 4751
- [41] Ohnesorge R, Löwen H and Wagner H 1994 *Phys. Rev. E* **50** 4801
- [42] Ball P C and Evans R 1988 *J. Chem. Phys.* **89** 4412
- [43] Henderson J R 1994 *Phys. Rev. E* **50** 4836
- [44] Hansen J-P and McDonald I R 1986 *Theory of Simple Liquids* 2nd edn (London: Academic)
- [45] Allen M P and Tildesley D J 1989 *Computer Simulation of Liquids* (Oxford: Clarendon)
- [46] Baus M, Rull L F and Ryckaert J P (ed) 1995 *Observation, Prediction and Simulation of Phase Transitions in Complex Fluids* (Dordrecht: Kluwer)
- [47] Jaster A 1998 *Europhys. Lett.* **42** 277
- [48] Weber H, Marx D and Binder K 1995 *Phys. Rev. B* **51** 14636
- [49] Lindemann F A 1910 *Z. Phys.* **14** 609
- [50] Ohnesorge R, Löwen H and Wagner H 1993 *Europhys. Lett.* **22** 245
- [51] Heni M and Löwen H 1999 *Phys. Rev. E* **60** 7057
- [52] It has been shown by
Evans R and Dijkstra M 2000 private communication
that capillary condensation affects the system close to bulk freezing for box lengths below $(30-40)\sigma$ but becomes negligible for greater box lengths as well as for positions further away from the bulk freezing point.
- [53] Biben T, Ohnesorge R and Löwen H 1994 *Europhys. Lett.* **28** 665
- [54] Löwen H and Beier T 1990 *Phys. Rev. B* **41** 4435
- [55] Löwen H 1990 *Phys. Rev. Lett.* **64** 2104
- [56] Rosenfeld Y 1998 *Mol. Phys.* **94** 929